Chen, K., Ge, M., Babeyko, A. Y., Li, X., Diao, F., Tu, R. (2016): Retrieving real-time co-seismic displacements using GPS/GLONASS: a preliminary report from the September 2015 M w 8.3 Illapel earthquake in Chile. - *Geophysical Journal International*, *206*, 2, pp. 941—953.

DOI: http://doi.org/10.1093/gji/ggw190

Geophysical Journal International

Geophys. J. Int. (2016) **206,** 941–953
Advance Access publication 2016 May 19
GJI Seismology

doi: 10.1093/gji/ggw190

Retrieving real-time co-seismic displacements using GPS/GLONASS: a preliminary report from the September 2015 M_w 8.3 Illapel earthquake in Chile

Kejie Chen,[1] Maorong Ge,[1] Andrey Babeyko,[1] Xingxing Li,[1] Faqi Diao[2] and Rui Tu[3]

[1] *GFZ German Research Center for Geosciences,* 14473 *Potsdam, Germany. E-mail: kejie@gfz-potsdam.de*
[2] *State Key Laboratory of Geodesy and Earth's Dynamics, Institute of Geodesy and Geophysics, Chinese Academy of Sciences, Wuhan* 430077*, China*
[3] *Chinese Academy of National Timing Service Center, Shu Yuan Road,* 710600 *Xi'an, China*

Accepted 2016 May 16. Received 2016 May 13; in original form 2016 January 28

SUMMARY

Compared with a single GPS system, GPS/GLONASS observations can improve the satellite visibility, optimize the spatial geometry and improve the precise positioning performance. Although the advantage over GPS-only methods in terms of positioning is clear, the potential contributions of GPS/GLONASS to co-seismic displacement determination and the subsequent seismic source inversion still require extensive study and validation. In this paper, we first extended a temporal point positioning model from GPS-only to GPS/GLONASS observations. Using this new model, the performance of the GPS/GLONASS method for obtaining co-seismic displacements was then validated via eight outdoor experiments on a shaking table. Our result reveals that the GPS/GLONASS method provides more accurate and robust co-seismic displacements than the GPS-only observations in a non-optimal observation environment. Furthermore, as a case study, observation data recorded during the September 2015 M_w 8.3 Illapel earthquake in Chile were re-processed. At some stations, obvious biases were found between the co-seismic displacements derived from GPS-only and GPS/GLONASS observations. The subsequent slip distribution inversion on a curved fault confirms that the differences in the co-seismic displacements causes differences in the inversion results and that the slip distributions of the Illapel earthquake inferred from the GPS/GLONASS observations tend to be shallower and larger.

Key words: Satellite geodesy; Transient deformation; Earthquake ground motions; Early warning.

1 INTRODUCTION

The potential of using GPS to retrieve co-seismic displacements was discussed as early as decades ago (see, e.g. Hirahara *et al.* 1994; Tsuji *et al.* 1995; Ge 1999; Ge *et al.* 2000). These early studies first experimentally demonstrated that GPS was able to capture transient co-seismic deformation. Following these pioneering studies, GPS has been widely exploited in monitoring seismic waveforms and extracting co-seismic offsets (see, e.g. Simons *et al.* 2002; Larson *et al.* 2003; Bock *et al.* 2004; Vigny *et al.* 2005; Banerjee *et al.* 2007). Consequently, an interdisciplinary subject of study, namely GPS seismology, was put forward (Larson 2009). Based on the near-real-time co-seismic displacements derived from GPS, seismic characteristics (e.g. magnitude, centroid location and slip distribution) can be inverted and can contribute to earthquake early warning and tsunami early warning systems, a current research hotspot (see, e.g. Blewitt *et al.* 2006; Sobolev *et al.* 2007; Allen & Ziv 2011; Li *et al.* 2013a,b; Melgar *et al.* 2013, 2016b; Melgar & Bock 2015; Riquelme *et al.* 2015). Compared with the traditional seismograph approach, the GPS sensor does not saturate and provides ground displacements without limits; thus, it is especially valuable for near-field tsunami early warning systems (Blewitt *et al.* 2009).

As a matter of fact, GPS is just one component of the Global Navigation Satellite Systems (GNSSs). With respect to the determination of co-seismic displacements, however, in most cases, only GPS is currently utilized. This is understandable considering that only GPS and the Global Navigation Satellite System (GLONASS) built by Russia currently offer global coverage. Moreover, GPS is the oldest and the most mature system, and the related error models and products, for example, satellite antenna phase centre offset, satellite orbit and clock biases, are the most precise. As a result, for many GNSS-based networks (e.g. GEONET in Japan and PBO in U.S.), most of the receivers have only received and recorded GPS signals over the past years.

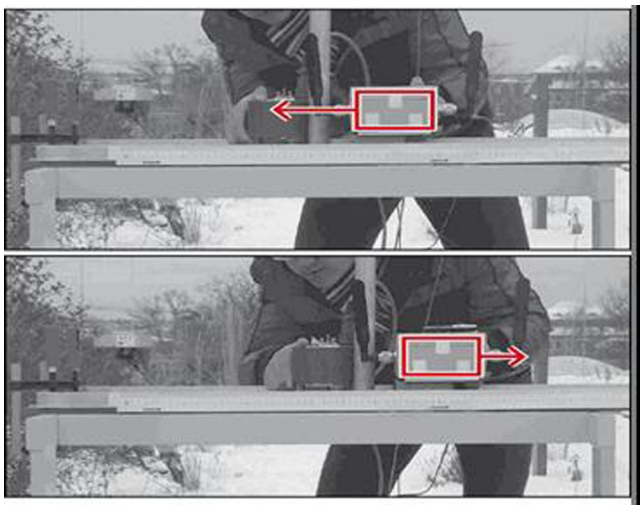

Figure 1. Experimental platform and illustration of the experiment in this study.

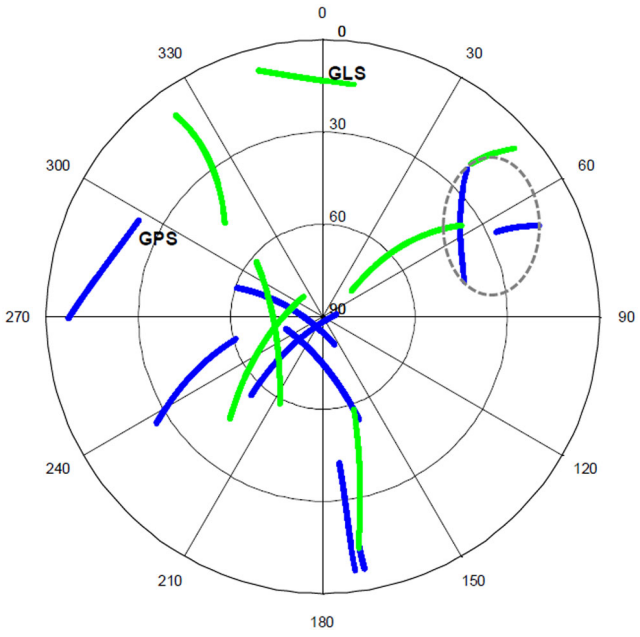

Figure 2. Sky view of the GPS/GLONASS constellations during the experiment period: the blue lines denote GPS satellites and the green lines represent GLONASS satellites. The two GPS satellites in the grey ellipse are excluded for a simulation scenario.

Currently, both GPS and GLONASS are undergoing modernization, and other navigation satellite systems, for example, Galileo built by the European Union and BeiDou built by China, have also been pilot tested or are providing regional service (see, e.g. Hofmann-Wellenhof *et al.* 2007; Yang *et al.* 2014). In total, there will be over 100 navigation satellites available, which improves observation redundancy significantly. Compared with a single system, a multi-GNSS can significantly improve the satellite visibility, optimize the spatial geometry, reduce dilution of precision and greatly benefit both scientific applications and engineering services (Li *et al.* 2015). Accordingly, the Multi-GNSS Experiment has been initiated by the International GNSS Service to pave the way for providing accurate products for all constellations (Montenbruck *et al.* 2014). Thus, the multi-GNSS era is coming.

While numerous previous studies have focused on using a single GPS system to obtain co-seismic displacements (see, e.g. Shi *et al.* 2010; Colosimo *et al.* 2011; Li *et al.* 2013a,b; Chen *et al.* 2015a), in this paper, we tested the performance of using GPS/GLONASS for co-seismic displacement retrieval and subsequent seismic source inversion as a pioneering case study of a multi-GNSS method for seismic hazard applications. In Section 2, the mathematical model of obtaining co-seismic displacements based on GPS/GLONASS observations is described. In Section 3, first, the results of eight outdoor experiments are shown for validation, then GPS/GLONASS data recorded during the September 2015 Illapel earthquake in Chile were re-processed and analysed in detail. In addition, the slip distribution inversion based on co-seismic offsets derived from GPS-only and GPS/GLONASS methods were conducted. Finally, Section 4 summarizes the main results and presents an outlook.

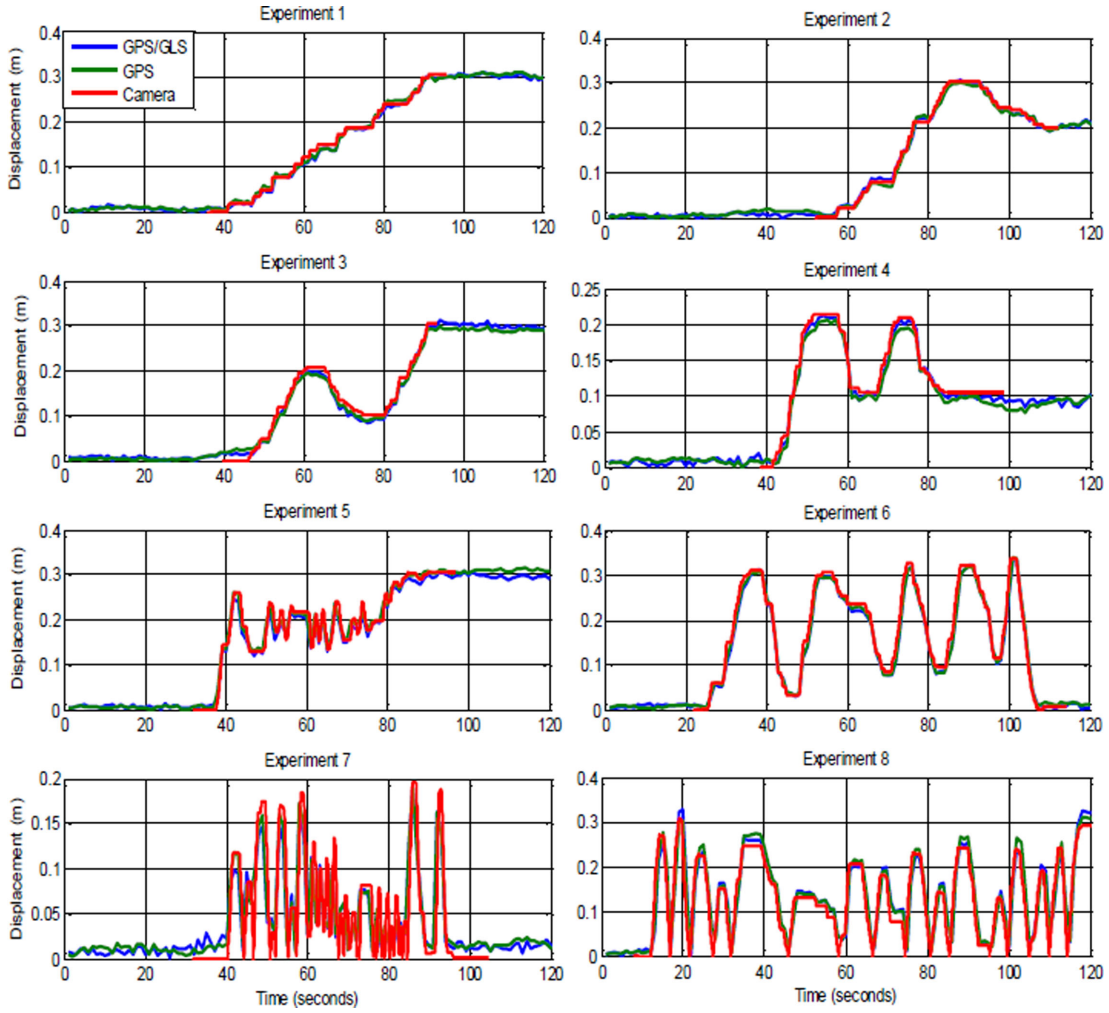

Figure 3. Displacements of the eight experiments retrieved from GPS/GLONASS, GPS-only and camera recordings.

2 GPS/GLONASS MODEL TO RETRIEVE REAL-TIME CO-SEISMIC DISPLACEMENTS

In the context of GPS/GLONASS constellations, the combined GPS+GLONASS observation model can be written as follows:

$$\begin{cases} L_{r,j}^{G} = \rho_{rg}^{G} - t^{G} + t_r + \lambda_{jG}(b_{rG,j} - b_j^{G}) + \lambda_{jG} N_{r,j}^{G} - \kappa_{jG} \cdot I_{r,1}^{G} + T_r^{G} + \varepsilon_{r,j}^{G} \\ L_{r,j}^{R_k} = \rho_{rg}^{R} - t^{R} + t_r + \lambda_{jR_k}(b_{rR_k,j} - b_j^{R}) + \lambda_{jR_k} N_{r,j}^{R} - \kappa_{jR_k} \cdot I_{r,1}^{R} + T_r^{R} + \varepsilon_{r,j}^{R} \\ P_{r,j}^{G} = \rho_{rg}^{G} - t^{G} + t_r + c(d_{rG,j} - d_j^{G}) + \kappa_{jG} \cdot I_{r,1}^{G} + T_r^{G} + e_{r,j}^{G} \\ P_{r,j}^{R_k} = \rho_{rg}^{R} - t^{R} + t_r + c(d_{rR_k,j} - d_j^{R}) + \kappa_{jR_k} \cdot I_{r,1}^{R} + T_r^{R} + e_{r,j}^{R} \end{cases} \quad (1)$$

where the indices G, R refer to the GPS and GLONASS systems, respectively, and R_k represents the GLONASS satellite with a frequency factor k; r and j denote the receiver and frequency, respectively; ρ_{rg} is the geometric distance from the satellite to the receiver; t^G, t^R and t_r represent the clock biases; λ is the wavelength of the corresponding frequency; b is the receiver and satellite un-calibrated phase delay; N is the integer ambiguity; c is the speed of light in vacuum; d is the code biases for receiver and satellite; I is the ionospheric delay; T is the slant tropospheric delay; and ε is the sum of the measurement noise and multipath error for the carrier phase and pseudo-range observations. With regard to other error budgets, for example, tidal loading, phase centre offsets and variations, the phase wind-up must be corrected according to the existing models as well.

Please note, because the signal frequencies and structures are different for each system, the code biases d_{rG}, d_{rR_k} are also different in each GPS/GLONASS receiver. Specially, for GLONASS satellites with different frequency factors, the receiver code biases d_{rR_k} are also different. To eliminate the differences between the receiver clock and code bias, the code bias for GPS satellites is usually set zero.

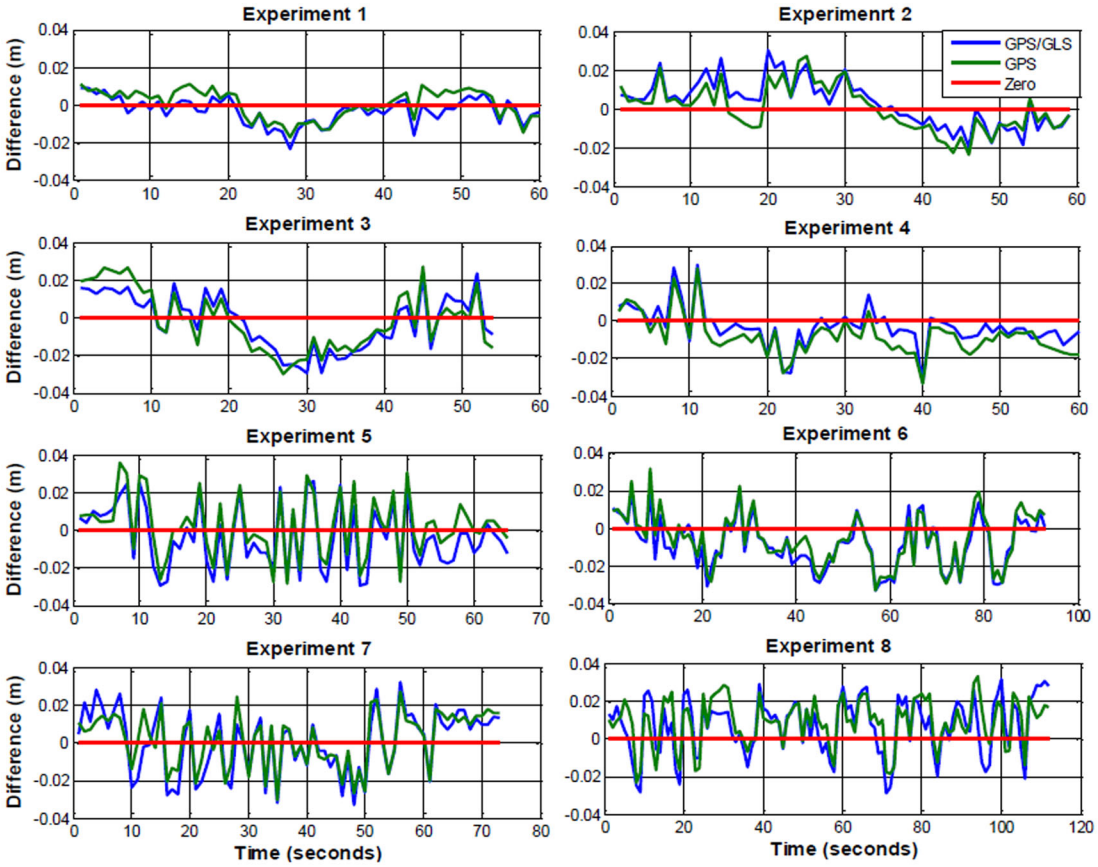

Figure 4. Differences between displacements derived from GPS/GLONASS, GPS-only and camera recordings.

Eq. (1) can be rewritten as follows:

$$\begin{cases} l_{r,j}^{G} = -u_r^{G} \cdot x + t_r + \lambda_{jG}(b_{rG,j} - b_j^{G}) + \lambda_{jG} N_{r,j}^{G} - \kappa_{jG} \cdot I_{r,1}^{G} + T_r^{G} + \varepsilon_{r,j}^{G} \\ l_{r,j}^{R_k} = -u_r^{R_k} \cdot x + t_r + \lambda_{jR_k}(b_{rR_k,j} - b_j^{R}) + \lambda_{jR_k} N_{r,j}^{R} - \kappa_{jR_k} \cdot I_{r,1}^{R} + T_r^{R} + \varepsilon_{r,j}^{R} \\ p_{r,j}^{G} = -u_r^{G} \cdot x + t_r + c(d_{rG,j} - d_j^{G}) + \kappa_{jG} \cdot I_{r,1}^{G} + T_r^{G} + e_{r,j}^{G} \\ p_{r,j}^{R_k} = -u_r^{G} \cdot x + t_r + c(d_{rR_k,j} - d_j^{R}) + \kappa_{jR_k} \cdot I_{r,1}^{R} + T_r^{R} + e_{r,j}^{R} \end{cases} \tag{2}$$

where $l_{r,j}^{s}$ and $p_{r,j}^{s}$ denote the 'observed minus computed' phase and pseudo-range observables, respectively. u_r^{s} denotes the unit vector from satellite s to receiver r, and x denotes the vector of position increments relative to *a priori* position x_0, which is used for linearization. For Temporal Point Positioning (TPP), proposed by Li *et al.* (2013a), precise satellite orbits and clocks are used, and the related errors are neglected in the two equations. By taking into account that pseudo-ranges are used mainly for initializing receiver clock bias in precise positioning, they are omitted in the following equations for simplicity.

Following the TPP approach, assuming that the position increment at the epoch t_0 (before the earthquake) is $x(t_0)$, the ambiguities N_{t0} can be estimated along with the receiver clock $t_r(t_0)$ and tropospheric delay $T(t_0)$ (fixed to an *a priori* model) at this epoch as follows:

$$\begin{cases} t_r(t_0) + \lambda_{jG}(b_{rG,j}(t_0) - b_j^{G}(t_0)) + \lambda_{jG} N_{r,j}^{G}(t_0) + T_r^{G}(t_0) = l_{r,j}^{G}(t_0) + u_r^{G}(t_0) \cdot x(t_0) - \varepsilon_{r,j}^{G}(t_0) \\ t_r(t_0) + \lambda_{jR_k}(b_{rR_k,j}(t_0) - b_j^{R}(t_0)) + \lambda_{jR_k} N_{r,j}^{R}(t_0) + T_r^{R}(t_0) = l_{r,j}^{R_k}(t_0) + u_r^{R}(t_0) \cdot x(t_0) - \varepsilon_{r,j}^{R}(t_0) \end{cases} \tag{3}$$

Assuming that the ambiguities are unchanged over the time of interest, if an epoch difference is formed between t_0 and t_n (after the earthquake breaks), we obtain the following:

$$\begin{cases} \Delta l_{r,j}^{G}(t_0, t_n) + u_r^{G}(t_0) \cdot x(t_0) - \varepsilon_{r,j}^{G}(t_n) = u_r^{G}(t_n) \cdot x(t_n) - \Delta t_r(t_0, t_n) - \Delta T_r^{G}(t_0, t_n) \\ \Delta l_{r,j}^{R}(t_0, t_n) + u_r^{R}(t_0) \cdot x(t_0) - \varepsilon_{r,j}^{R}(t_n) = u_r^{R}(t_n) \cdot x(t_n) - \Delta t_r(t_0, t_n) - \Delta T_r^{R}(t_0, t_n) \end{cases} \tag{4}$$

Here, we can see that it is cancelled out through epoch differencing, which is one special advantage that should be emphasized because the inter-system/inter-frequency bias does not have impact on the TPP strategy.

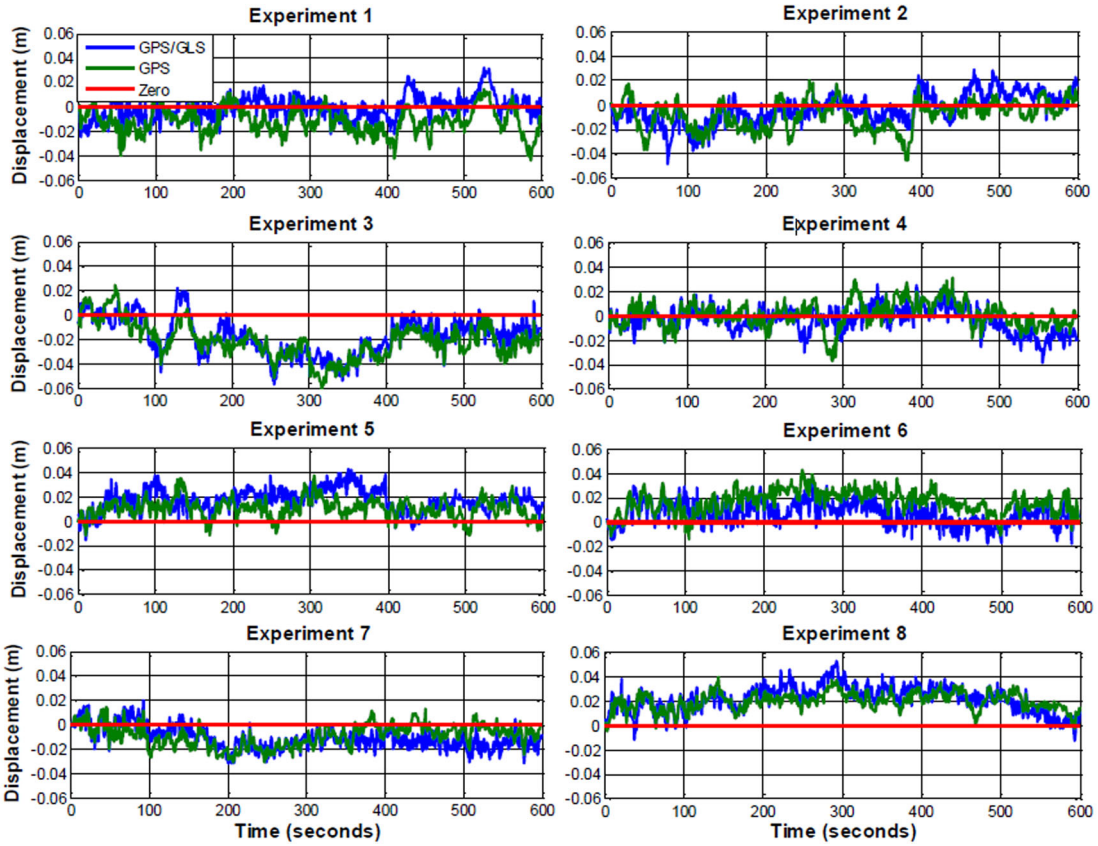

Figure 5. Vertical displacements retrieved from the GPS/GLONASS and GPS-only data. Please note that the benchmark of the vertical displacements is zero.

Usually, the station position is precisely known (millimetre- to centimetre-level accuracy) for the epoch before the earthquake breaks, that is, $x(t_0)$can be treated as zero. Thus, eq. (4) can be rewritten as follows:

$$\begin{cases} \Delta l^G_{r,j}(t_0,t_n) - \varepsilon^G_{r,j}(t_n) + \Delta T^G_r(t_0,t_n) = u^G_r(t_n)\cdot x(t_n) - \Delta t_r(t_0,t_n) \\ \Delta l^R_{r,j}(t_0,t_n) - \varepsilon^R_{r,j}(t_n) + \Delta T^R_r(t_0,t_n) = u^R_r(t_n)\cdot x(t_n) - \Delta t_r(t_0,t_n) \end{cases} \tag{5}$$

As clearly shown in eq. (5), the accuracy of the relative position change $X(t_n)$ is mainly affected by variation in the tropospheric delay from epoch t_0 to t_n. Promisingly, after correction with an empirical model (e.g. Saastamoinen 1972), the tropospheric delay residual is limited to several centimetres (Schüler 2014). Moreover, due to the spatial and temporal correlation, the tropospheric delay can be further reduced through epoch differencing. Thus, for a few tens of minutes, $\Delta T(t_0,t_n)$ is expected to be at the centimetre level. Consequently, the estimation of $x(t_n)$ is presumed to be at the centimetre level as well.

For weighting of the observations, the classical elevation-dependent model is adopted:

$$P = \begin{cases} 2\cdot\sin(E) & E \le 30^\circ \\ 1 & E > 30^\circ \end{cases} \tag{6}$$

Here, E is the elevation angle. Finally, with regard to real-time precise GPS/GLONASS clock and orbit determinations, we follow the same procedure as described in (Li *et al.* 2015).

3 PERFORMANCE ASSESSMENT OF GPS/GLONASS FOR RETRIEVING REAL-TIME CO-SEISMIC DISPLACEMENTS

In this contribution, the application of GPS/GLONASS to obtain co-seismic displacements, was first analysed based on an outdoor experimental platform and then tested using data from the 2015 Illapel earthquake in Chile.

3.1 Outdoor experimental validation

To better validate the performance of GPS/GLONASS in retrieving co-seismic displacements, outdoor experimental 1 Hz GPS/GLONASS data recorded in December 2012 by Tu & Chen (2014) were first reprocessed in a real-time scenario and analysed in detail. The antenna was

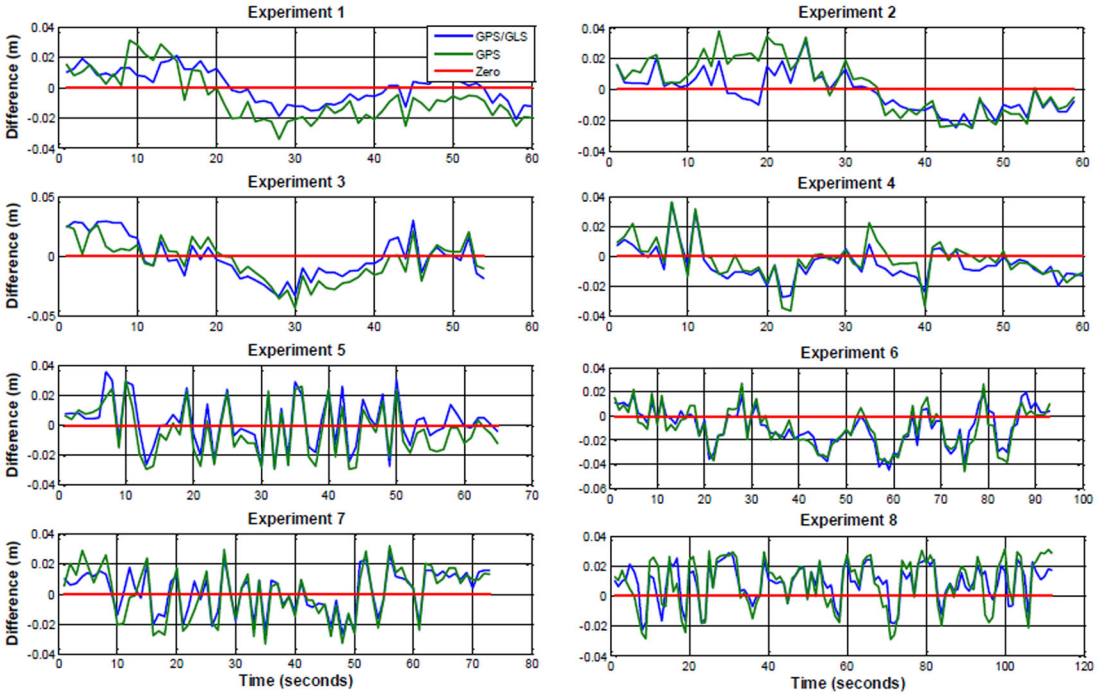

Figure 6. Differences among the displacements derived from the GPS/GLONASS and GPS-only data with two GPS satellites masked relative to the camera recordings.

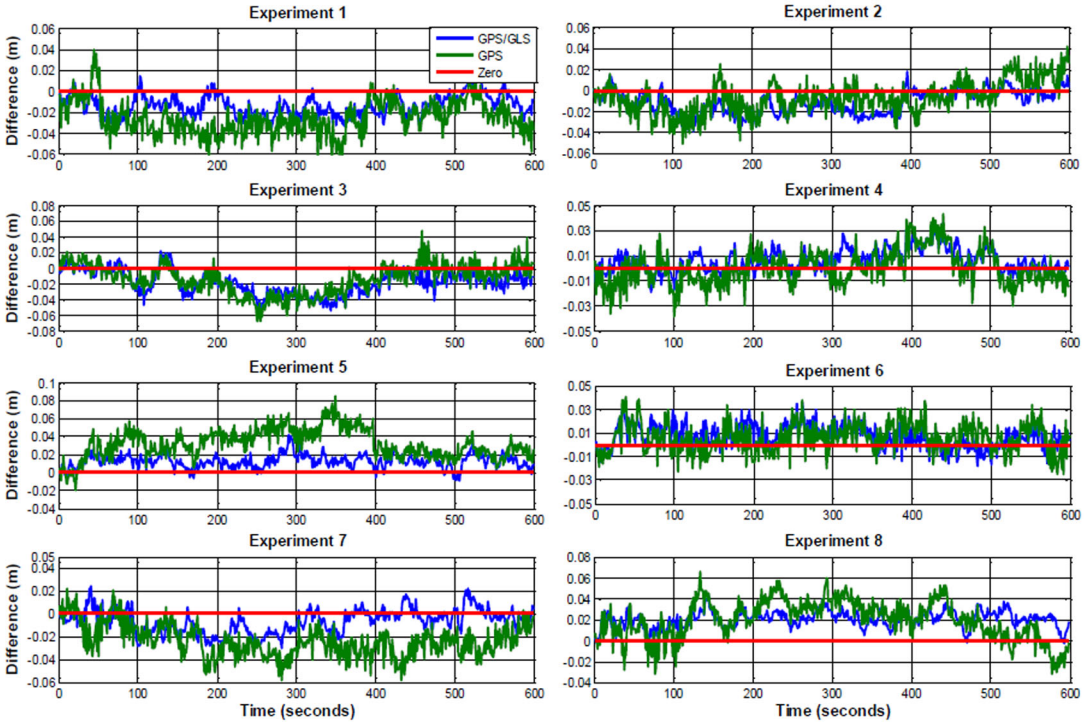

Figure 7. Vertical displacements retrieved from the GPS and GPS/GLONASS data with two GPS satellites masked. Please note that the benchmark of the vertical displacements is zero.

pushed forward and backward along a horizontal straight track (see Fig. 1). In total, there were eight individual experiments with movements of different frequencies and amplitudes. For comparison, the antenna motion was also captured by a camera at 25 fps (frames per second) with a pixel resolution of 3 mm, and the displacements revealed from the camera were set as benchmarks.

As a precise position of the station before the movement is crucial for the TPP method, 3 hr of GPS/GLONASS data collected before the motion started was processed in static PPP mode to obtain cm level antenna position. Then, GPS-only data and GPS/GLONASS data were processed using TPP. The sky view of the observed satellites during the experimental period is depicted in Fig. 2. As clearly shown,

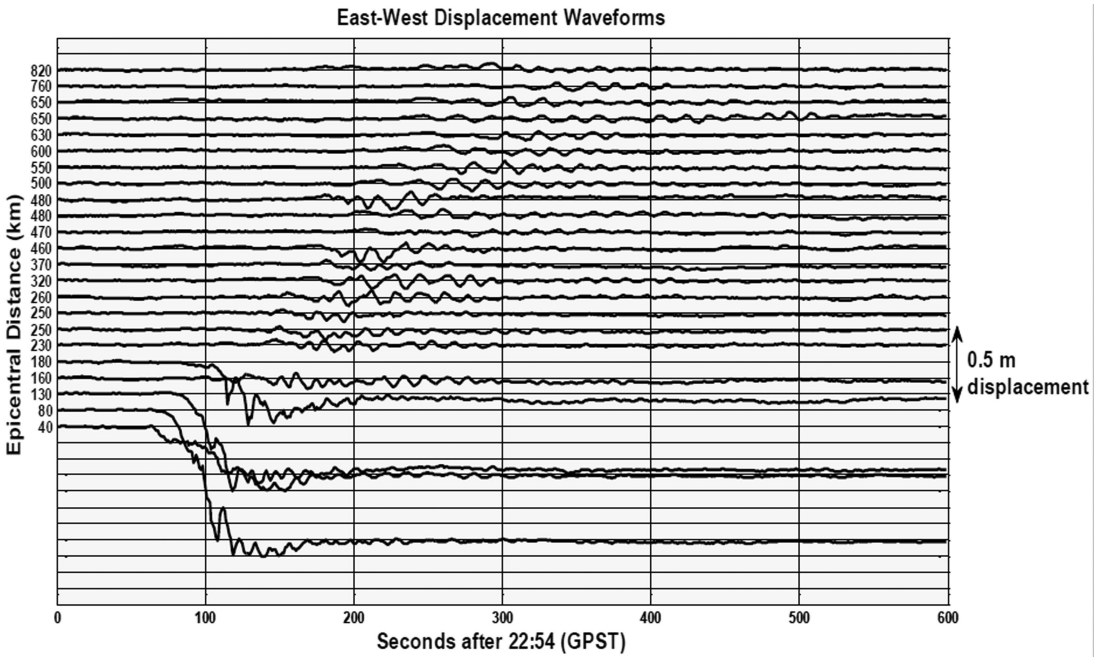

Figure 8. East–west components of 1 Hz displacement waveforms estimated from TPP using GPS/GLONASS observations. The plot is sorted by the epicentral distance of each station.

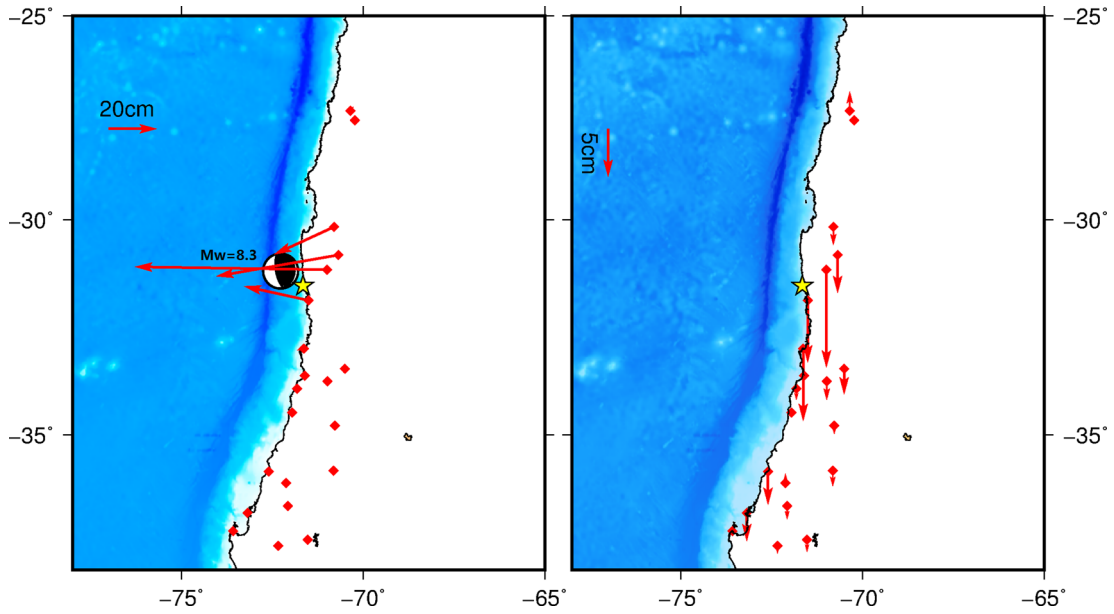

Figure 9. Distribution of monitoring stations and co-seismic displacements derived from GPS/GLONASS. The left subplot is horizontal and the right one is vertical. The yellow star and the beach ball show the epicentre and focal mechanism provided by the USGS.

the GPS-only satellites show a good geometry with nine evenly distributed GPS satellites in view. Taking into account that the camera recorded total displacements, we converted the east–west and north–south motion components derived from GPS and GPS/GLONASS to displacements.

The corresponding results are shown in Fig. 3. The displacements from the GPS/GLONASS, GPS-only and camera recordings show a high degree of consistency. Setting the camera recordings as the benchmarks, the horizontal displacement differences are shown in Fig. 4, and the vertical displacement differences are shown in Fig. 5. The statistical accuracies of the GPS/GLONASS and GPS-only data are both 0.012 m in the horizontal and are 0.017 and 0.018 m in the vertical, respectively.

However, an optimal distribution of GPS satellites similar to this study cannot always be guaranteed in practice. To simulate adverse observation conditions, two GPS satellites were excluded (see in Fig. 2), and the new TPP results from GPS/GLONASS and GPS-only are presented in Figs 6 and 7. Not surprisingly, the displacements feature more evident differences between the GPS-only and camera observations. Nonetheless, the GPS/GLONASS results are more robust and closer to the benchmark. As a matter of fact, in this scenario, the accuracies

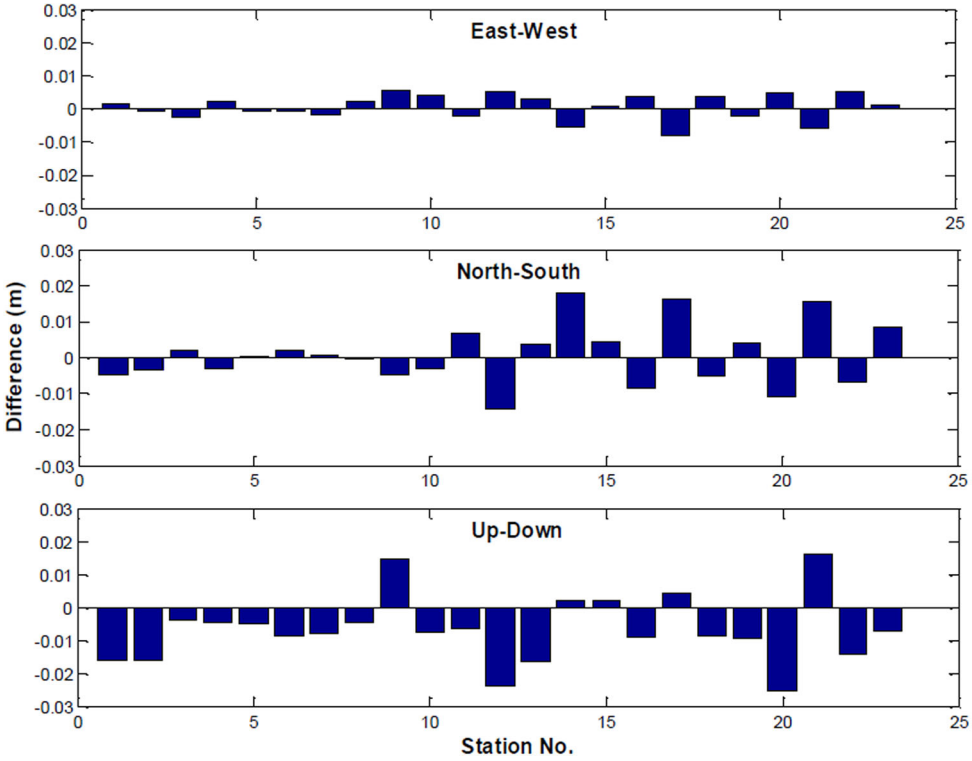

Figure 10. Co-seismic static displacements differences between GPS/GLONASS and GPS-only, from top to bottom: east–west component, north–south component, up–down component.

of the GPS/GLONASS and GPS-only data are 0.013 and 0.018 m, respectively, for the horizontal components and 0.020 and 0.029 m, respectively, for the vertical components.

Through the outdoor experiments, it is concluded that GLONASS contributes slightly to positioning accuracy in situations where sufficient GPS satellites are tracked. However, when positioning is conducted in adverse conditions, for example, GPS signal blockages, adding a couple of GLONASS satellites can improve the GPS satellite geometry and consequently improve positioning reliability, availability and accuracy significantly.

3.2 A case study of the September 2015 M_w 8.3 Illapel earthquake in Chile

While many earthquakes have been recorded by real-time GPS arrays and analysed intensively by previous studies, few have been recorded by GPS/GLONASS arrays. Thus, limited data are available for validation of the GPS/GLONASS combination performance. In this paper, our example is observation data from the 2015 September 16 M_w 8.3 Illapel earthquake, and the high-rate GPS/GLONASS data were provided by the Centro Sismológico Nacional, Universidad de Chile. The megathrust event occurred at 22:54 (UTC) as the result of thrust faulting along the interface between the Nazca and South America plates in central Chile. A notable tsunami was triggered and observed along the coast of Coquimbo and the cities of Coquimbo (http://www.ioc-sealevelmonitoring.org/).

In total, 23 continuous GPS/GLONASS stations with excellent spatial coverage near the epicentre (see Fig. 8) were replayed using TPP in a simulated real-time mode, and the precise GPS/GLONASS orbit and clock data were calculated using the Position And Navigation Data Analysis (PANDA) software following the strategies described in Li *et al.* (2015). On average, the number of visible satellites during this period increased from eight (GPS-only) to fourteen (GPS/GLONASS). To extract permanent deformation from the derived displacement waveforms, we applied a 100 s moving average to each displacement record in each coordinate component. The static displacements were determined on-the-fly by differencing the average value and the nominal starting position (position at 10 s before the theoretical *P*-wave arrival time), and the process lasted until differences between the neighbouring obtained static offsets were less than 1 cm. The displacement waveforms and final permanent displacements from GPS/GLONASS are shown in Figs 8 and 9. Moreover, the differences between displacements obtained from GPS/GLONASS and from GPS-only are shown in Fig. 10.

Fig. 8 clearly shows that the co-seismic offsets at most of the stations are not obvious (less than 5 cm), whereas the four stations located closest to the epicentre experienced more significant shaking. Fig. 10 indicates that the scale of the co-seismic offset differences vary from station to station. At some stations, the differences are negligible. However, the biases could be up to 2 cm in the horizontal direction and almost 3 cm in the vertical direction at some other stations. To explore the possible reasons, the stations LNQM (where the difference is small) and TAMR (where the difference is large) are analysed in detail. In Figs 11 and 12, we show the satellite sky views at station LNQM

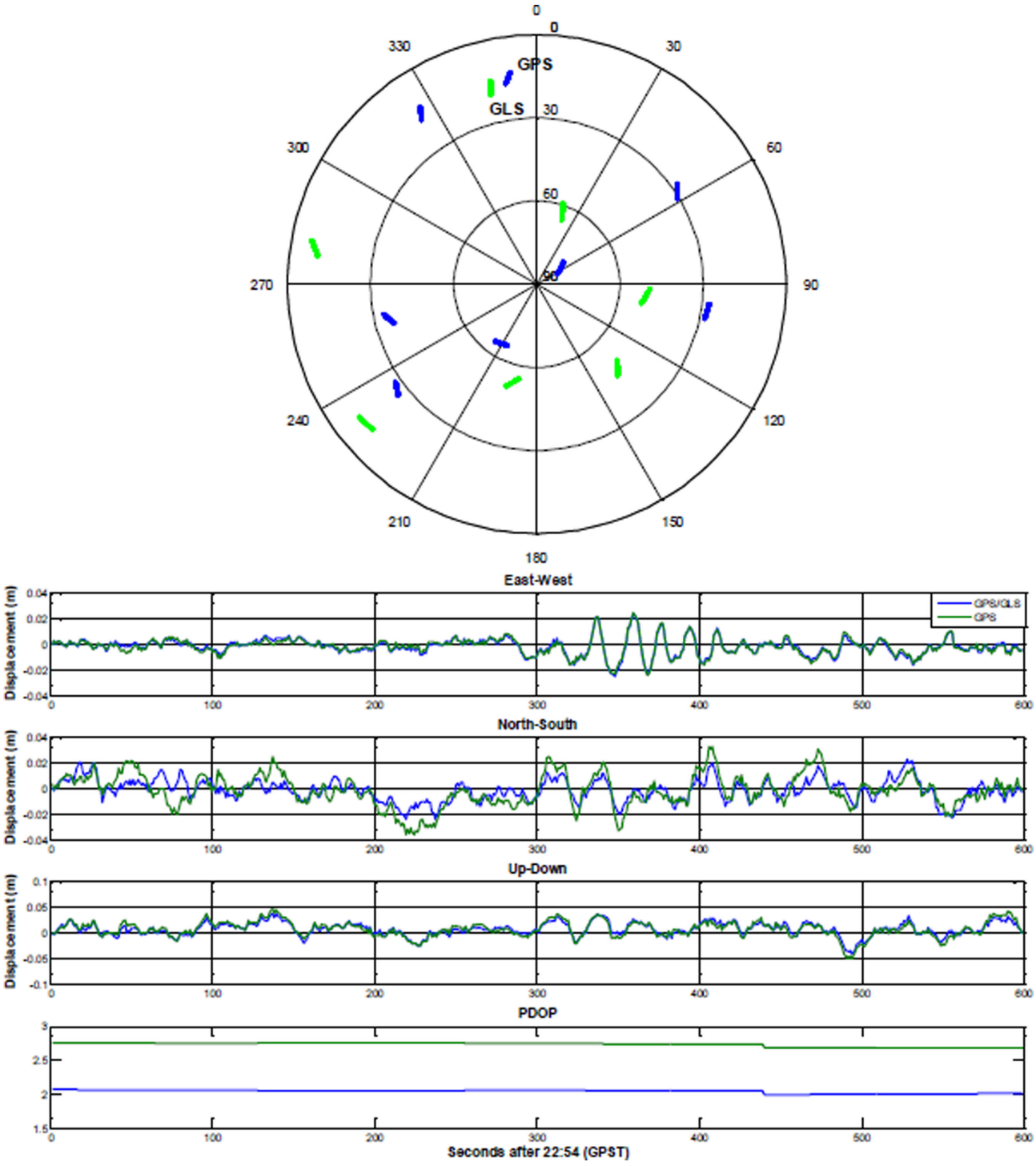

Figure 11. Sky view of station LNQM and co-seismic displacements retrieved from the GPS/GLONASS and GPS observations, together with PDOP.

and TAMR together with the co-seismic displacement waveforms derived from the GPS/GLONASS and GPS-only observations. In addition, positional dilution of precision (PDOP) is also present.

As Figs 11 and 12 show, for station LNQM, there were eight GPS satellites observed during the earthquake time, and the PDOP is 2.7 on average, which indicate ideal observation conditions. In this case, even though adding seven GLONASS satellites can reduce PDOP to 2.1 on average, there are almost no differences in the co-seismic displacement waveform retrieval. In contrast, at station TAMR, six GPS satellites were tracked, and the PDOP is 3.2 on average. Having four more GLONASS satellites in view improves the constellation geometry greatly (PDOP is reduced to 2.2 on average), leading to biases in the co-seismic displacement retrieval.

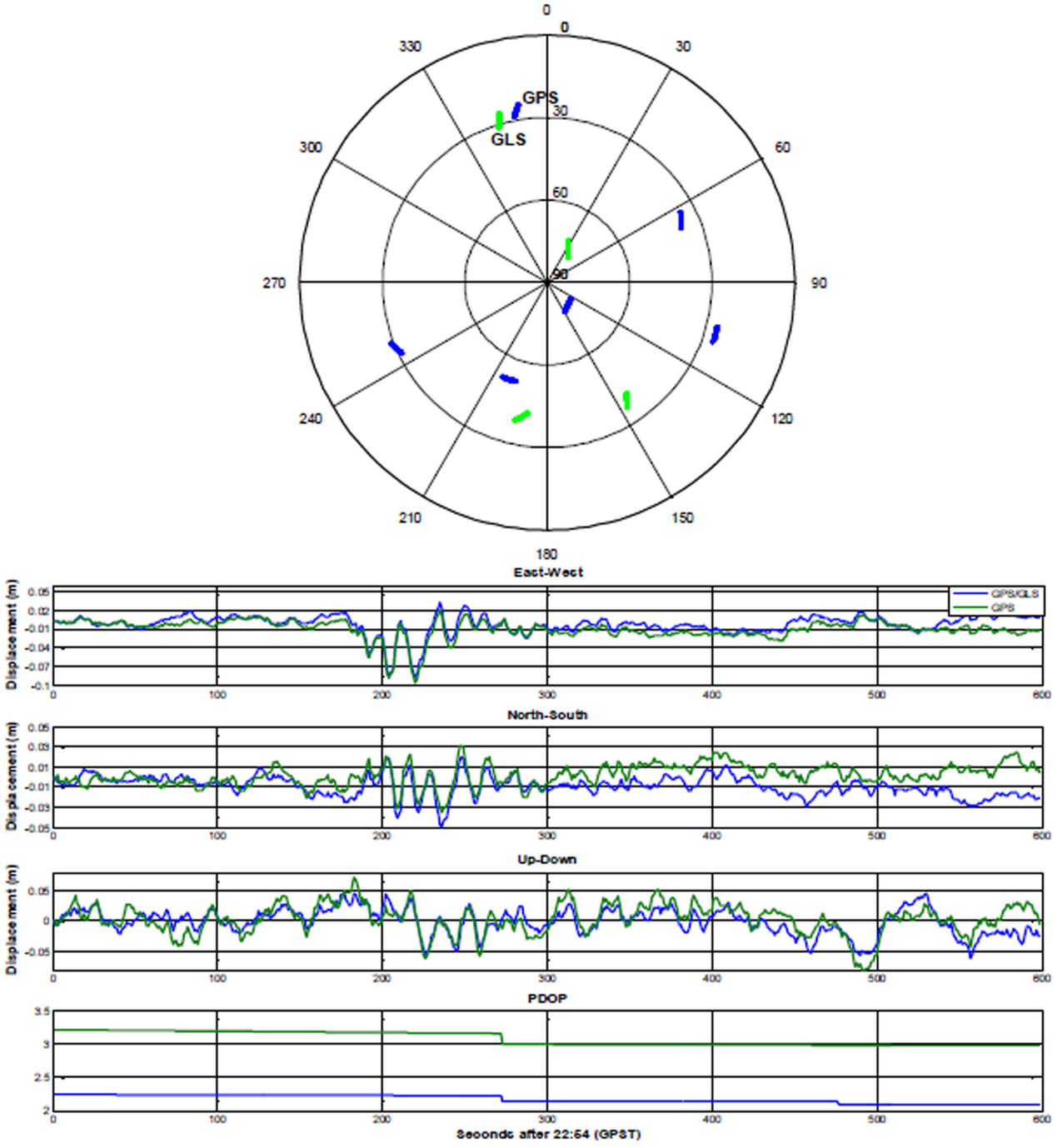

Figure 12. Sky view of station TAMR and co-seismic displacements retrieved from the GPS/GLONASS and GPS observations, together with PDOP.

3.3 Slip distribution inversions

For a geo-hazard early warning system, a high-resolution slip model should be inverted once the near-field co-seismic offsets are determined, thereby playing an important role further in other applications, for example, tsunami early warning and seismic hazard assessments. As the results show in Section 3.2, clear differences were observed between the static offsets based on the GPS/GLONASS and GPS-only observations. To determine how and to what extent these differences affect the inferred slip distribution, several inversions were performed and the results were compared. Constrained by the solved co-seismic displacements, the well-developed Steepest Descent Method (Wang *et al.* 2009, 2013) inversion code was applied to invert for slip distribution on a predefined 3-D plate interface. A curved fault geometry, inferred from the SLAB 1.0 model (Hayes *et al.* 2012), was assumed to be the rupture fault and was then discretized into 330 rectangular fault patches. The layered crustal model CRUST 5.1 (Mooney *et al.* 1998) was implemented beneath the surface stations to compute the Green's

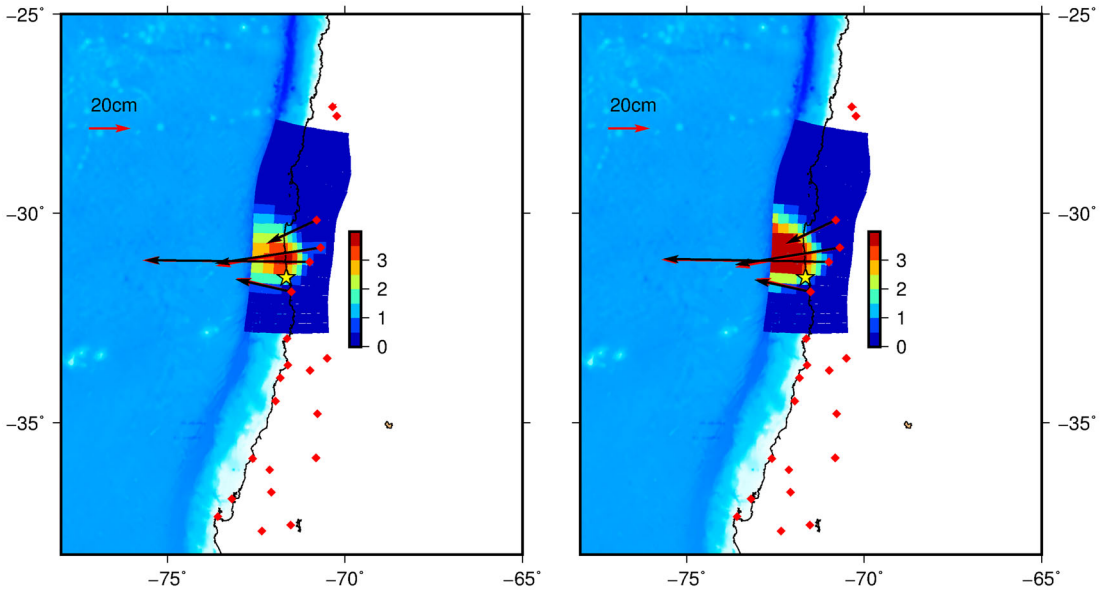

Figure 13. Slip inversions based on co-seismic displacements from GPS (left) and GPS/GLONASS (right) using a curved fault with 330 individual patches. The red vectors denote observed co-seismic static offsets, and the black ones represent synthetic values.

function. We used the trade-off curve method as described in Diao *et al.* (2011) to fix the smoothing factor in the inversion. The final slip distributions inverted from co-seismic offsets are shown in Fig. 13.

The derived slip models are generally consistent in terms of moment magnitude, rupture scales and location. The moment magnitude of the earthquake inferred from GPS-only observations is 8.22, with a max slip of 3.91 m and a mean slip of 0.49 m. In comparison, the inverted moment magnitude from GPS/GLONASS observations is slightly larger (8.25), with a max slip of 4.50 m and a mean slip of 0.57 m. Most importantly, the latter slip distributions tend to be shallower and towards the trench, which may produce a greater tsunami wave height in the scenario of a geo-hazard early warning system.

In addition, both slip models fit the observed data pretty well. To be exact, for the GPS-only case, the root mean square (RMS) residuals in the north–south, east–west and vertical directions are 0.8, 0.9 and 2.6 cm, respectively. For the GPS/GLONASS case, the RMS residuals are 0.7, 0.8 and 1.6 cm, respectively. In general, the model predictions better explain the observations from GPS/GLONASS in the vertical direction, suggesting a higher observation precision of this system.

4 DISCUSSION AND CONCLUSIONS

In this study, we extended the TPP from GPS-only to GPS/GLONASS observations and tested the performances of the GPS/GLONASS in co-seismic displacement retrieval through outdoor experiments. Compared with the GPS-only system, GPS/GLONASS has more visible satellites and optimizes the constellation spatial geometry, and it has the advantage of providing more robust and accurate co-seismic displacements, especially when the GPS-only observations are not ideal.

The case study of the September 2015 Illapel earthquake in Chile reveals that the biases between the co-seismic displacements derived from GPS-only and GPS/GLONASS observations vary from station to station and could be up to 2 cm in the horizontal direction and almost 3 cm in the vertical direction. The analyses show that there is an evident relationship between the bias scales and the satellites observed. For example, when only six GPS satellites were tracked and the PDOP of the GPS-only observations is relatively large, adding several GLONASS satellites can lead to significant differences in the co-seismic displacement determination. Considering the results from the outdoor experiments, we believe that the co-seismic displacements obtained from GPS/GLONASS are closer to the true values.

Subsequent slip distribution inversion on a curved fault confirms that the differences in the co-seismic displacements cause variations in the inversion results. The slip distributions of the Illapel earthquake inferred from the GPS/GLONASS observations tend to be shallower and larger, which implies a greater tsunami impact. Nonetheless, it should also be noted that for the slip distribution inversions, besides co-seismic displacements, there are other options that can affect the inversion results, for example, the inversion algorithm implemented, the GPS/GLONASS array distribution, and the fault geometry. However, it should mentioned that the inversion results shown in Section 3.3 were derived from the same inversion frame (fault geometry, earth structure and inversion parameter). For example, if we use a single rectangular fault and run the inversion again, the differences are found to be negligible (see Fig. 14). However, it should be mentioned that the inversion results shown in Section 3.3 were derived from a more realistic inversion frame (a curved fault geometry and a layered earth structure). The only difference is the input co-seismic displacements captured by the GPS/GLONASS system and GPS-only system. We therefore infer that the differences between the inverted slip models are mainly induced by input observations, which highlights the importance of utilizing more precise observations.

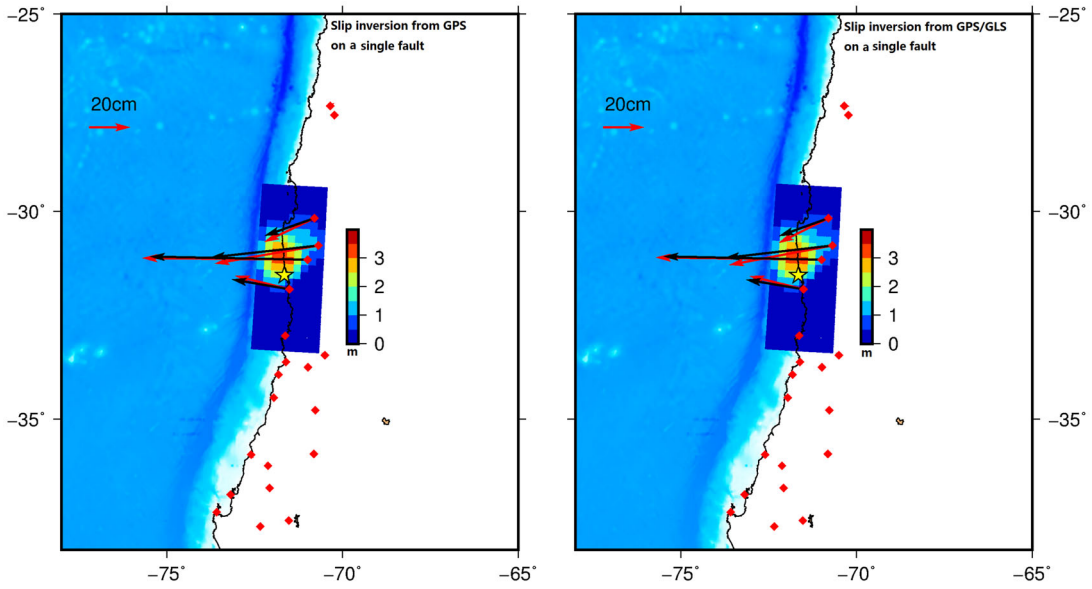

Figure 14. Slip inversions based on co-seismic displacements from GPS and GPS/GLONASS on a single fault consisting of 23 × 9 uniform patches. The length and width of the fault are 450 and 190 km, respectively. The strike angle is set as 4°, and the dip angle is set as 19°. The red vectors denote observed co-seismic static offsets, and the black ones represent synthetic values.

Furthermore, other inversion results (e.g. Melgar *et al.* 2016a) show observable differences compared with our results in terms of peak slip and detailed slip pattern, though the rupture scale and moment magnitude show general agreement. They carried out a joint inversion by employing local high-rate GPS records, strong motion seismograms, InSAR data and tide gauge records, which should yield a more comprehensive model. However, perhaps only a few sources of data (high-rate GPS data and strong motion seismograms) are available for near-real-time inversions, and the resolution of inversion results (as shown by this study) may suffer from the limited dataset. To provide a rapid response and tsunami early warning, a more robust estimation of rupture scale and moment magnitude is perhaps imperative (Diao *et al.* 2016), whereas more details are necessary for studies on rupture dynamics. In fact, as the recent work of Melgar *et al.* (2016a,b) and Chen *et al.* (2016) shows, if we just focus on tsunami early warning, the tsunami scenarios are similar, in spite of the differences in source inversions.

Because GLONASS employs Frequency Division Multiple Access for signal transmission, which leads to integer ambiguity resolution difficulty, the accuracy of the obtained GLONASS orbit and clock data is not as good as that of GPS. Recently, Liu *et al.* (2015) proposed a new method to improve the GLONASS precise orbit determination, and it is expected to improve GPS/GLONASS precise positioning.

In addition to GPS/GLONASS, recent studies (Chen *et al.* 2015b; Geng *et al.* 2015) have demonstrated the feasibility of using BeiDou for earthquake and tsunami monitoring in the Asia-Pacific region. The TPP model can be easily extended to the GPS/GLONASS/BeiDou/GALILEO systems once data recorded during earthquake by the four systems is publicly available, and the application of multi-GNSS for geo-hazard monitoring could then be evaluated.

ACKNOWLEDGEMENTS

Kejie Chen is financially supported by China Scholarship Council (CSC) for his PhD study at GFZ. Authors acknowledge the support by the German Federal Ministry for Education and Research (BMBF) under grant agreement No. 01DN12089. High-rate GNSS data were provided by the Centro Sismológico Nacional, Universidad de Chile. This study was also supported by the National Natural Science Foundation of China (Grant Nos. 41504006 and 41304017). We appreciate the valuable comments from Dr Sebastian Riquelme and the other anonymous reviewer, which improved this manuscript greatly. The authors also thank Diego Melgar for helpful discussions.

REFERENCES

Allen, R.M. & Ziv, A., 2011. Application of real-time GPS to earthquake early warning, *Geophys. Res. Lett.,* **38,** 1–7.

Banerjee, P., Pollitz, F., Nagarajan, B. & Bürgmann, R., 2007. Coseismic slip distributions of the 26 December 2004 Sumatra–Andaman and 28 March 2005 Nias earthquakes from GPS static offsets, *Bull. seism. Soc. Am.,* **97,** S86–S102.

Blewitt, G., Kreemer, C., Hammond, W.C., Plag, H.-P., Stein, S. & Okul, E., 2006. Rapid determination of earthquake magnitude using GPS for tsunami warning systems, *Geophys. Res. Lett.,* **33,** L11309–L11309.

Blewitt, G., Hammond, W.C., Kreemer, C., Plag, H.-P., Stein, S. & Okul, E., 2009. GPS for real-time earthquake source determination and tsunami warning systems, *J. Geod.,* **83,** 335–343.

Bock, Y., Prawirodirdjo, L. & Melbourne, T.I., 2004. Detection of arbitrarily large dynamic ground motions with a dense high-rate GPS network, *Geophys. Res. Lett.,* **31**(6), doi:10.1029/2003GL019150.

Chen, K., Ge, M., Li, X., Babeyko, A., Ramatschi, M. & Bradke, M., 2015a. Retrieving real-time precise co-seismic displacements with a standalone single-frequency GPS receiver, *Adv. Space Res.,* **56**(4), 634–647.

Chen, K., Zamora, N., Babeyko, A.Y., Li, X. & Ge, M., 2015b. Precise positioning of BDS, BDS/GPS: implications for Tsunami early warning in South China Sea, *Remote Sens.,* **7,** 15 955–15 968.

Chen, K., Babeyko, A., Hoechner, A. & Ge, M., 2016. Comparing source inversion techniques for GPS-based local tsunami forecasting: a case study for the April 2014 M8.1 Iquique, Chile earthquake, *Geophys. Res. Lett.,* **43,** 3186–3192.

Colosimo, G., Crespi, M. & Mazzoni, A., 2011. Real-time GPS seismology with a stand-alone receiver: a preliminary feasibility demonstration, *J. geophys. Res.,* **116**(B11), doi:10.1029/2010JB007941.

Diao, F., Xiong, X., Ni, S., Zheng, Y. & Ge, C., 2011. Slip model for the 2011 M_w 9.0 Sendai (Japan) earthquake and its M_w 7.9 aftershock derived from GPS data, *Chin. Sci. Bull.,* **56,** 2941–2947.

Diao, F., Wang, R., Aochi, H., Walter, T.R., Zhang, Y., Zheng, Y. & Xiong, X., 2016. Rapid kinematic finite-fault inversion for an M_w 7+ scenario earthquake in the Marmara Sea: an uncertainty study, *Geophys. J. Int.,* **204**(2), 813–824.

Ge, L., 1999. GPS seismometer and its signal extraction, in *Proc. 12th Int. Tech. Meeting of the Satellite Division of the US Inst. of Navigation GPS ION'99,* Nashville, TN.

Ge, L. *et al.*, 2000. GPS seismometers with up to 20 Hz sampling rate, *Earth Planets Space,* **52,** 881–884.

Geng, T., Xie, X., Fang, R., Su, X., Zhao, Q., Liu, G. & Liu, J., 2015. Real-time capture of seismic waves using high-rate multi-GNSS observations: application to the 2015 M_w 7.8 Nepal earthquake, *Geophys. Res. Lett.,* **43,** 161–167.

Hayes, G.P., Wald, D.J. & Johnson, R.L., 2012. Slab1.0: a three-dimensional model of global subduction zone geometries, *J. geophys. Res.,* **117,** B01302–B01302.

Hirahara, K, Nakano, T & Hoso, Y., 1994. An experiment for GPS strain seismometer, in *Japanese Symposium on GPS,* Tokyo, Japan, pp. 67–75.

Hofmann-Wellenhof, B., Lichtenegger, H. & Wasle, E., 2007. *GNSS–Global Navigation Satellite Systems: GPS, GLONASS, Galileo, and More,* Springer Science & Business Media.

Larson, K.M., 2009. GPS seismology, *J. Geod.,* **83,** 227–233.

Larson, K.M., Bodin, P. & Gomberg, J., 2003. Using 1-Hz GPS data to measure deformations caused by the Denali fault earthquake, *Science,* **300,** 1421–1424.

Li, X., Ge, M., Guo, B., Wickert, J. & Schuh, H., 2013a. Temporal point positioning approach for real-time GNSS seismology using a single receiver, *Geophys. Res. Lett.,* **40,** 5677–5682.

Li, X., Ge, M., Zhang, X., Zhang, Y., Guo, B., Wang, R., Klotz, J. & Wickert, J., 2013b. Real-time high-rate co-seismic displacement from ambiguity-fixed precise point positioning: application to earthquake early warning, *Geophys. Res. Lett.,* **40,** 295–300.

Li, X., Ge, M., Dai, X., Ren, X., Fritsche, M., Wickert, J. & Schuh, H., 2015. Accuracy and reliability of multi-GNSS real-time precise positioning: GPS, GLONASS, BeiDou, and Galileo, *J. Geod.,* **89,** 607–635.

Liu, Y, Ge, M, Shi, C., Lou, Y., Wickert, J. & Schuh, H., 2015. Improving GLONASS precise orbit determination through data connection, *Sensors,* **15,** 30 104–30 114.

Melgar, D. & Bock, Y., 2015. Kinematic earthquake source inversion and tsunami runup prediction with regional geophysical data. *J. Geophys. Res. Solid Earth,* **120,** 3324–3349.

Melgar, D, Crowell, B.W, Bock, Y. & Haase, J.S., 2013. Rapid modeling of the 2011 M_w 9.0 Tohoku-oki earthquake with seismogeodesy, *Geophys. Res. Lett.,* **40,** 2963–2968.

Melgar, D., Fan, W., Riquelme, S., Geng, J., Liang, C., Fuentes, M. & Fielding, E.J., 2016a. Slip segmentation and slow rupture to the trench during the 2015, M_w 8. 3 Illapel, Chile earthquake, *Geophys. Res. Lett.,* **43,** 961–966.

Melgar, D. *et al.*, 2016b. Local tsunami warnings: perspectives from recent large events, *Geophys. Res. Lett.,* **43,** 1109–1117.

Montenbruck, O., Steigenberger, P., Khachikyan, R., Weber, G., Langley, R.B., Mervart, L. & Hugentobler, U., 2014. IGS-MGEX: preparing the ground for multi-constellation GNSS science, *Inside GNSS,* **9,** 42–49.

Mooney, W.D, Laske, G. & Masters, T.G., 1998. CRUST 5.1: A global crustal model at 5 × 5, *J. geophys. Res.,* **103,** 727–747.

Riquelme, S., Fuentes, M., Hayes, G.P. & Campos, J., 2015. A rapid estimation of near-field tsunami runup, *J. geophys. Res.,* **120**(9), 6487–6500.

Saastamoinen, J., 1972. Atmospheric correction for the troposphere and stratosphere in radio ranging satellites, in *The Use of Artificial Satellites for Geodynamics*, pp. 247–251, eds Henriksen, S.W., Mancini, A. & Chovitz, B.H., American Geophysical Union.

Schüler, T., 2014. The TropGrid2 standard tropospheric correction model, *GPS Solut.,* **18,** 123–131.

Shi, C, Lou, Y., Zhang, H., Zhao, Q., Geng, J., Wang, R., Fang, R. & Liu, J., 2010. Seismic deformation of the M_w 8.0 Wenchuan earthquake from high-rate GPS observations, *Adv. Space Res.,* **46,** 228–235.

Simons, M., Fialko, Y. & Rivera, L., 2002. Coseismic Deformation from the 1999 M_w 7.1 Hector Mine, California, earthquake as inferred from InSAR and GPS observations, *Bull. seism. Soc. Am.,* **92,** 1390–1402.

Sobolev, S.V. *et al.*, 2007. Tsunami early warning using GPS-Shield arrays, *J. geophys. Res.,* **112,** B08415–B08415.

Tsuji, H., Hatanaka, Y., Sagiya, T. & Hashimoto, M., 1995. Coseismic crustal deformation from the 1994 Hokkaido-Toho-Oki earthquake monitored by a nationwide continuous GPS array in Japan, *Geophys. Res. Lett.,* **22**(13), 1669–1672.

Tu, R. & Chen, K., 2014. Tightly integrated processing of high-rate GPS and accelerometer observations by real-time estimation of transient baseline shifts, *J. Navig.,* **67,** 869–880.

Vigny, C. *et al.*, 2005. Insight into the 2004 Sumatra–Andaman earthquake from GPS measurements in southeast Asia, *Nature,* **436,** 201–206.

Wang, R., Diao, F. & Hoechner, A., 2013. SDM-A geodetic inversion code incorporating with layered crust structure and curved fault geometry, in *EGU General Assembly Conference Abstracts* Vol. 15, p. 2411.

Wang, L., Wang, R., Roth, F., Enescu, B., Hainzl, S. & Ergintav, S., 2009. Afterslip and viscoelastic relaxation following the 1999 M 7.4 İzmit earthquake from GPS measurements, *Geophys. J. Int.,* **178,** 1220–1237.

Yang, Y., Li, J., Wang, A., Xu, J.Y., He, H.B., Guo, H.R., Shen, J.F. & Dai, X., 2014. Preliminary assessment of the navigation and positioning performance of BeiDou regional navigation satellite system, *Sci. China Earth Sci.,* **57,** 144–152.